Article

Enhanced Mechanical Properties of CLAM by Zirconium Alloying and Thermo-Mechanical Processing

Dongping Zhan [1,*], Jihang Li [1], Dongwei Wang [1], Huishu Zhang [2,*], Guoxing Qiu [3] and Yongkun Yang [3]

1   School of Metallurgy, Northeastern University, Shenyang 110819, China
2   School of Metallurgy Engineering, Liaoning Institute of Science and Technology, Benxi 117004, China
3   School of Metallurgical Engineering, Xi'an University of Architecture and Technology, Xi'an 710055, China
*   Correspondence: zhandp1906@163.com (D.Z.); huishu_zhang@163.com (H.Z.)

Abstract: In this study, we present the effects of 0.004~0.098 wt% Zr and thermo-mechanical processing (TMP) on the microstructure and mechanical properties of the China RAFM steel, CLAM, as a feasibility study for improving mechanical properties. The inclusions in ingots were characterized using optical microscope (OM) and scanning electron microscope (SEM), which could be classified as fine simple particles and large complex particles. The complexity of the alloy's inclusion composition increases with the increasing Zr concentration. The higher the Zr content, the more complex the composition of inclusions in the alloy. The average diameter of inclusions in 0.004Zr steel was the smallest, which was 0.79 μm and the volume fraction was 0.018%. The highest yield strength, tensile strength, elongation, and impact energy of 0.004Zr alloy at room temperature were 548.3 MPa, 679.4 MPa, 25.7%, and 253.9 J. The structure of the TMPed steels was all tempered martensite. With the increase in tempering temperature, the yield and tensile strength of the experimental steel gradually decreased, while the elongation and impact energy gradually increased. The 0.004ZrD and 0.004ZrH alloys had the best yield strength and impact energy, which were 597.9 and 611.8 MPa and 225.9 and 243.3 J, respectively. In addition, the alloys showed good thermal stability during the aging at 600 °C for 1500 h. It was discovered that TMP is a simple and practical industrial technique that could successfully enhance the mechanical properties of CLAM steel without sacrificing impact toughness.

Keywords: China low activation martensitic steel; Zr; inclusion; thermo-mechanical processing; mechanical properties

1. Introduction

Reduced activated ferrite/martensitic (RAFM) steel has been considered as a candidate structural material for fusion blanket due to its excellent thermal conductivity, low coefficient of thermal expansion, and better resistance to expansion [1,2]. RAFM steel was developed to achieve low activation capacity by replacing Mo, Nb, and Ni with W and Ta in conventional ferritic-martensitic 8–12% CrMoVNb steel [3,4]. Several series of RAFM steels have been developed since the 1980s, including CLAM [5] and CLF-1 [6] from China, Eurofer97 [7] from Europe, F82H and JLF-1 [8] from Japan, 9Cr-2WVTa [9] from America, and EK-181 [10] from Russia.

Since 2011, the Korea Atomic Energy Research Institute has studied 98 different components of Eurofer97 steel [11]. The yield strength of alloy with 0.005 wt% Zr was slightly reduced, but the impact properties were significantly improved due to the solution softening effect of Zr. Moreover, the existence of MnS inclusions on preformed ZrO_2 and the formation of intragranular ferrite lead to the increase in impact toughness of high-strength low alloy pipeline steel with Zr [12]. The ZrB_2 inclusion in Zr-containing low-carbon steel could refine grains by the pinning effect to increase the high-temperature strength of the alloy [13]. Chun et al. [14] developed ARAA steel containing Zr with similar properties to Eurofer97 by vacuum induction melting using the solution strengthening effect of Zr in

steel. All the results showed that Zr demonstrates great potential in improving mechanical properties and modifying oxides in alloys. However, the strengthening mechanism of Zr is still unclear and needs to be further studied.

At present, extensive studies have been conducted to enhance the properties of RAFM steels [15,16]. Thermal mechanical processing (TMP) is a method to control the microstructure of the steel by changing the rolling process parameters without changing the composition of the steel [17]. In various hot working processes, hot rolling at temperatures below A_{C1} can significantly improve the yield strength and tensile strength of alloys by refining grain and carbide deposits and increasing dislocation density. In the tempering process, the dislocations and other defects introduced in the rolling process could provide more nucleation sites for carbides, which is more conducive to the precipitation of carbides.

In this work, 0.004–0.098 wt% Zr were added to investigate the effect of Zr addition on the inclusions and microstructure of CLAM steel, in order to improve the mechanical properties of this steel. In addition, the effects of deformation temperature and tempering temperature on microstructure and mechanical properties, such as yield strength and impact resistance, were studied. The results of this work can provide experience for the process design of RAFM steels for improving mechanical properties.

2. Materials and Experiments

2.1. Materials

Four CLAM steels with different Zr were produced in a 25 kg vacuum induction melting furnace. The chemical compositions of the steels were listed in Table 1. Based on the Zr content, these steels were named 0Zr, 0.004Zr, 0.037Zr, and 0.098Zr steels. Electrolytic Cr, pure W, Ta, and Fe were placed into the magnesia crucible before the power was turned on. Before melting, the vacuum in the furnace was reduced to 20 Pa. These raw materials were melted at ~1550 °C under vacuum for 1 h to ensure a uniform mixture. Then, pure Si, electrolytic Mn, pure V, and sponge Zr were added sequentially at 1 min intervals. The molten alloy was cast into steel ingot at 1520 °C under the protection of argon (0.3 MPa).

Table 1. Chemical compositions of experimental steels (wt%).

Steel	C	Si	Mn	Cr	W	V	Ta	N	O	Zr	Fe
0Zr	0.06	0.1	0.45	9	1.5	0.2	0.15	0.0030	0.0043	-	Bal.
0.004Zr	0.06	0.1	0.45	9	1.5	0.2	0.15	0.0025	0.0032	0.004	Bal.
0.037Zr	0.06	0.1	0.45	9	1.5	0.2	0.15	0.0023	0.0018	0.037	Bal.
0.098Zr	0.06	0.1	0.45	9	1.5	0.18	0.15	0.0022	0.0014	0.098	Bal.

After homogenization at 1200 °C for 1.5 h, these ingots were hot forged into 35 × 50 mm blocks at 950 to 1150 °C, then rolled in 4 passes and finally hot rolled (over the same temperature range) into 12-mm thick plates. All the rolling reductions (35 mm → 24 mm → 17 mm → 13.5 mm → 12 mm) were achieved in single passes. Rolling temperature and heat treatment could seriously affect the properties of steels. Different final rolling temperatures and heat treatment methods were designed, as shown in Table 2. Process A was used to evaluate the effect of Zr on the microstructure and mechanical properties of CLAM steel. The effect of TMP on the microstructure and mechanical properties was investigated by Process B~I. Finally, TMP-CLAM steel with Zr was aged at 600 °C for 1500 h to examine the microstructure stability.

Table 2. Rolling temperatures and heat treatment conditions and the designations.

Process	Start Rolling Temperature	Finish Rolling Temperature	Normalizing	Tempering
A		950 °C	1050 °C × 20 min	760 °C × 90 min
B				690 °C × 90 min
C				725 °C × 90 min
D		950 °C		760 °C × 90 min
E	1150 °C			795 °C × 90 min
F				690 °C × 90 min
G				725 °C × 90 min
H		750 °C		760 °C × 90 min
I				795 °C × 90 min

2.2. Microstructure and Mechanical Property Tests

Samples for inclusion statistics were cut from the ingot and their cross sections were polished. More than 49 optical microscope (OM) photographs at a magnification of 500 were used to determine the size and number of inclusions in the samples, using image analysis software (Image Pro Plus 6.0). The single field of view area is 453×453 μm^2, and the total observation area of each sample is greater than 1005 mm^2. Since inclusions in steel are mostly spherical and polygonal, the equivalent body diameter ($\bar{d}_V = \pi n / 2 \sum_{i=1}^{n} (1/d_{Ai})$ [18], where n is the measured number of inclusions in the total observation area and d_{Ai} is the diameter of each inclusion on the cross section) was used to determine the geometric size of inclusions. The number of inclusions per unit volume (N_V) could be assessed on the following relationship: $N_V = N_A / \bar{d}_V$ [18], where N_A is the number of particle sections per unit area. The number of particles per unit area (N_A) was calculated as follows: $N_A = n / A_{obs}$, where A_{obs} is the total observation area and n is the number of inclusions in A_{obs}. Volume fraction of spherical particles (f_V) is expressed as $f_V = (\pi/6) \cdot \bar{d}_V^3 \cdot N_V$ [18]. The inclusion and microstructure of the alloy were observed by scanning electron microscope (SEM) with energy dispersive spectrometer. Samples for observation of microstructure were prepared using 1% picric acid solution (1 g picric acid + 5 mL HCl + 100 mL CH_3CH_2OH). The precipitated phase powder in steel was obtained by electrolytic extraction with 10% ethanolic solution of hydrochloric acid at room temperature. The nickel plate was used as the inert electrode, the current was less than 0.8 A, and the electrolytic extraction time was more than 24 h. X-ray diffraction (XRD) analyzer was used to detect carbides.

A bar-type sample with a gauge section of 5.0 mm in diameter and 25 mm in length was used for the tensile test at room temperature with strain rate of 2 mm per min. The standard V-notch Charpy specimens sized $10 \times 10 \times 55$ mm were subjected to an impact test at room temperature. The reported data represent an average of three measurements for each condition.

3. Results and Discussion

3.1. Inclusions in Ingots

The morphology of typical inclusions in ingots with different Zr is shown in Figure 1, including simple inclusions (TaO_x, MnS, and ZrN) and composite inclusions (TaO_x-ZrO_2, ZrO_2-MnS, TaO_x-ZrN, and $FeZr_x$-ZrO_2). As shown in Figure 1a–i, the size of simple inclusions (TaO_x, MnS, and ZrN) is small, typically less than 2 μm. The size of composite inclusions (TaO_x-ZrO_2, ZrO_2-MnS, TaO_x-ZrN, and $FeZr_x$-ZrO_2) is relatively large, greater than 3 μm. In addition, most of the composite inclusions are Zr-rich oxide inclusions in the center. Sulfides and nitrides are usually precipitated during solidification. Therefore,

zirconia preferentially precipitated in steel may become the nucleating particles of sulfides and nitrides.
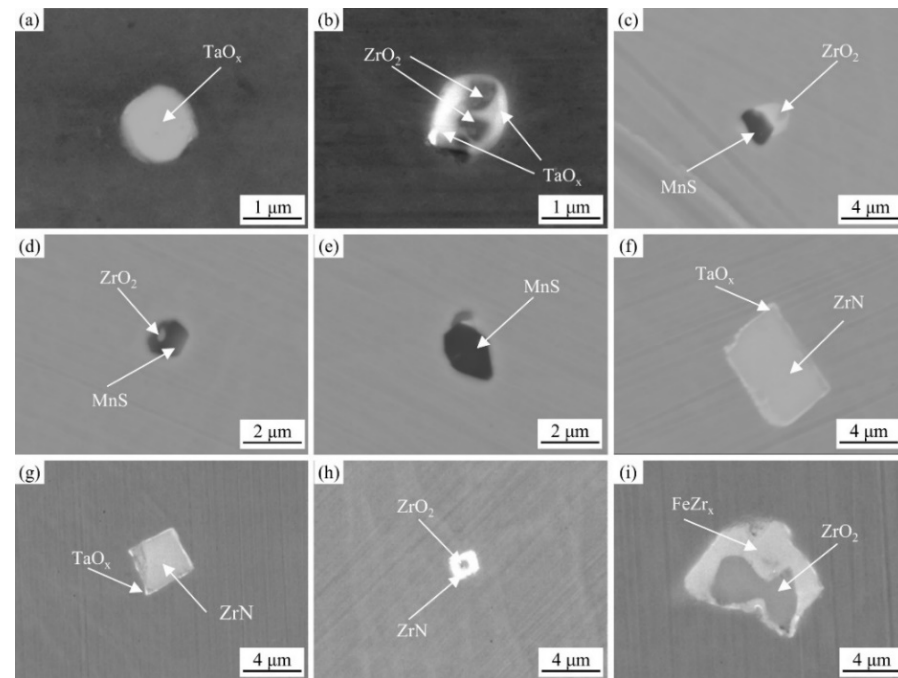

Figure 1. Morphology of typical inclusions in ingots. (**a**) 0Zr steel, (**b**,**c**) 0.004Zr steel, (**d**–**f**) 0.037Zr steel, and (**g**–**i**) 0.098Zr steel.

Table 3 shows the statistical results of inclusions in ingots. The proportion of 0.5~1 μm inclusions in 0.004Zr steel is clearly higher than 0Zr, 0.037Zr, and 0.098Zr steels, which is about two times the size of 0Zr. With the increase in Zr content in steel, the proportion of large-size inclusions clearly increases. The proportion of inclusions in the size of 1–3 μm in 0.037Zr steel increased and inclusions below 1 μm decreased. In contrast to 0Zr, 0.004Zr, and 0.037Zr steels, inclusions smaller than 0.5 μm and larger than 5 μm increased significantly in 0.098Zr alloy. The $\bar{d}_v$ of 0Zr, 0.004Zr, 0.037Zr, and 0.098Zr steels are 1.102, 0.788, 1.352, and 1.582 μm, respectively, whereas f_V of 0Zr, 0.004Zr, 0.037Zr, and 0.098Zr steels are 0.0065%, 0.0176%, 0.0253%, and 0.0336%, respectively. The inclusion in 0.004Zr steel is clearly smaller than the 0Zr, 0.037Zr, and 0.098Zr steels. Zr could significantly refine the inclusion in the CLAM steel, which was found in other RAFM steels [11,14].

Table 3. Statistical results of inclusions in ingots.

Steel	Size Distribution/%					$\bar{d}_v$ /μm	f_V /10^{-4}
	<0.5 μm	0.5–1.0 μm	1.0–3.0 μm	3.0–5.0 μm	>5 μm		
0Zr	6.23	40.46	40.40	11.15	1.76	1.10	0.65
0.004Zr	12.93	69.24	16.04	0.89	0.9	0.79	1.76
0.0037Zr	0.37	49.63	42.62	6.07	1.31	1.35	2.53
0.0098Zr	25.29	6.35	23.96	10.57	33.83	1.58	3.36

3.2. Microstructure of CLAM Steels with Zr

The microstructure of steels treated by Process A is shown in Figure 2. We have quantitatively counted the size of prior austenite grain in 0ZrA, 0.004ZrA, 0.037ZrA, and 0.098ZrA specimens. According to the statistical results of linear intercept method, the size of prior austenite grain in 0ZrA, 0.004ZrA, 0.037ZrA, and 0.098ZrA specimens has been determined to be 22.4, 20.3, 21.6, and 20.8 μm, respectively. The grain size of 0.004ZrA steel is the smallest, and the 0ZrA steel is the largest. With the addition of Zr, the grain size of the steels increased first and then decreased. As shown in Figure 2g,h, some large

Zr-rich inclusions were found in 0.037ZrA steel, and Zr-Ta-rich inclusions larger than 5 μm were found in 0.098ZrA steel. These inclusions are residual inclusions from ingots, which indicates that the hot working process (forging, rolling, normalizing, and tempering) has little effect on large Zr-rich and Zr-Ta-rich inclusions.
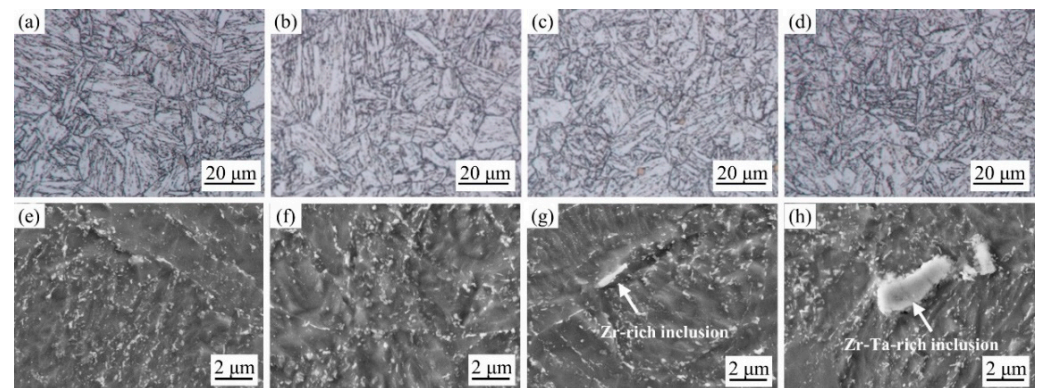

Figure 2. Microstructure of tempered steels. (**a**–**d**) OM, (**e**–**h**) SEM, (**a**,**e**) 0ZrA, (**b**,**f**) 0.004ZrA, (**c**,**g**) 0.037ZrA, and (**d**,**h**) 0.098ZrA.

Carbide precipitates are the most important precipitates in CLAM steels as a type of precipitated hardened alloy steel. Carbide precipitates in tempered steel not only increase the steel's strength and toughness through precipitation at room temperature, but also prevent the microstructure from coarsening at high temperature, effectively improving the high temperature strength and creep properties of the alloy [19]. Figure 3 shows XRD results of electrolytic extraction of precipitate with 10% ethanolic solution of hydrochloric acid. Typical precipitates, such as $M_{23}C_6$ and MX, could be found in 0ZrA and 0.004ZrA alloys. In addition to $M_{23}C_6$ and MX, some ZrO_2 exists in 0.037ZrA and 0.098ZrA alloys due to the high Zr content.
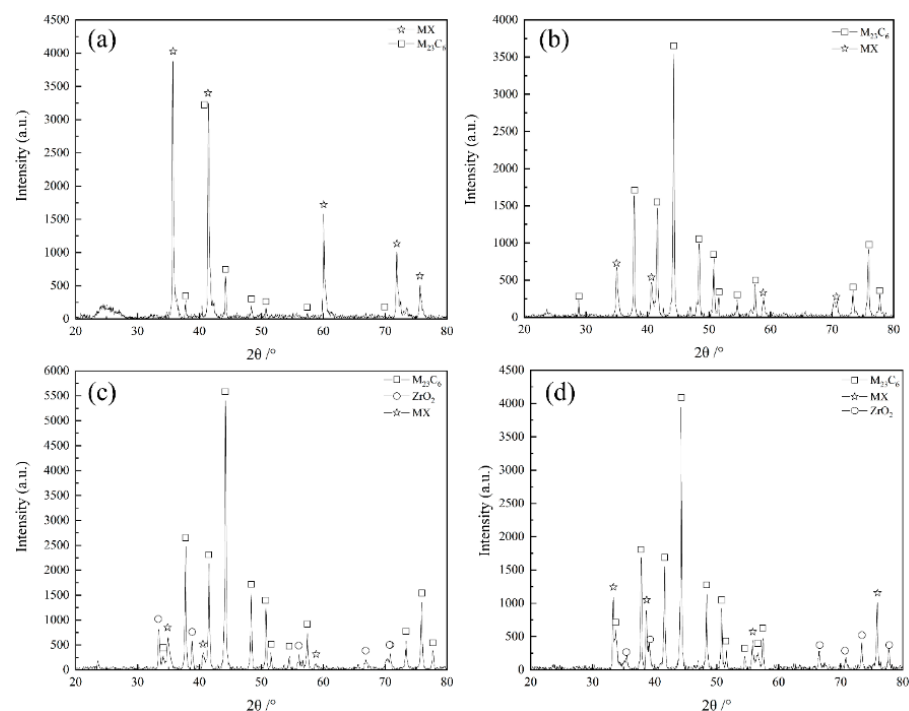

Figure 3. XRD results of precipitates in the steels. (**a**) 0ZrA, (**b**) 0.004ZrA, (**c**) 0.037ZrA, and (**d**) 0.098ZrA.

3.3. Mechanical Property of CLAM Steels with Zr

The mechanical properties of the steels treated by Process A are shown in Figure 4. The yield strengths (YS) of 0ZrA, 0.004ZrA, 0.037ZrA, and 0.098ZrA steels are 482.5, 548.3, 522.1, and 490.8 MPa, respectively. The tensile strengths (TS) are 610.9, 679.4, 660.5, and 625.7 MPa, respectively, and the elongations are 25.1%, 25.7%, 24.3%, and 21.1%, respectively. The alloy with the highest yield and tensile strength is the 0.004ZrA alloy with the minimum grain size and average diameter of inclusions. With the addition of Zr content, the yield strength, tensile strength, and elongation of the steel decrease. When the Zr content was increased to 0.094%, the strength and plasticity of 0.098ZrA alloy decreased significantly, which was mainly caused by the excessive number and density of large inclusions [20].
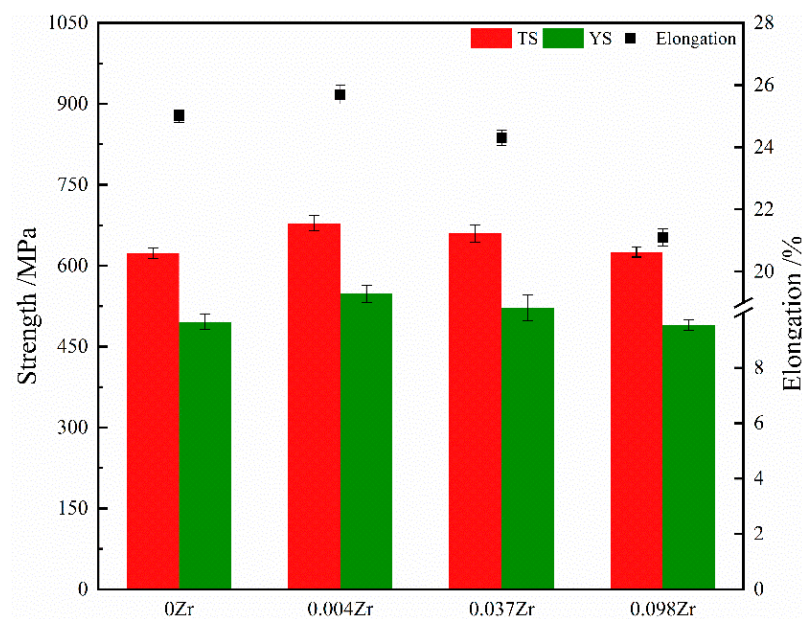

Figure 4. Tensile properties of CLAM steel with Zr. Error bars correspond to one standard deviation from the mean value.

Figure 5 shows the microscopic fracture morphology of steels at room temperature. All four steels exhibit plastic fracture during the tensile process; namely, clear "necking" occurs before the fracture. The fracture process of materials is the process of micropore formation, expansion, and transmission [21]. During the tensile process, the steel initially undergoes irreversible deformation, and stress concentration occurs around the matrix and inclusions, resulting in microcrack defects [22]. As the degree of deformation increases, the defects gradually expand and form micropores along the inclusions. The continuous expansion and connection of micropores eventually causes the material to fracture. As shown in Figure 5a, equiaxial fine dimples were evenly distributed in the tensile fracture of the 0ZrA steel due to the small inclusions. Dimples in 0.004ZrA steel were not only uniform but also deep, some small Zr oxides were found in the dimples, as shown in Figure 5b. Some large ZrN inclusions with square shape were found in the dimples of 0.037ZrA alloy, which made it easier to form a stress concentration in the tensile process [23], as shown in Figure 5c. Due to the uneven size distribution of inclusions in 0.098ZrA alloy, the sizes of depressions and particles were different in the microstructure of tensile fracture, as shown in Figure 5d. The inclusions in the small dimples are mainly Zr oxides, while the inclusions in the larger dimples are ZrN and $FeZr_x$-ZrO_2. During the tensile process, the nearly spherical Zr oxide could delay the expansion of micropores, compared with the angular ZrN and $FeZr_x$-ZrO_2, showing smaller dimples. Compared with 0ZrA, 0.004ZrA, and 0.037ZrA steels, inclusions in 0.098ZrA steel are not only larger in size and quantity, but also more apparent in aggregation. During the tensile process, micropores would be formed at the ZrN and $FeZr_x$-ZrO_2 inclusions due to the stress concentration, which then

expand and connect rapidly, and finally dimples with larger but relatively shallow size will be formed, as shown in Figure 5d.
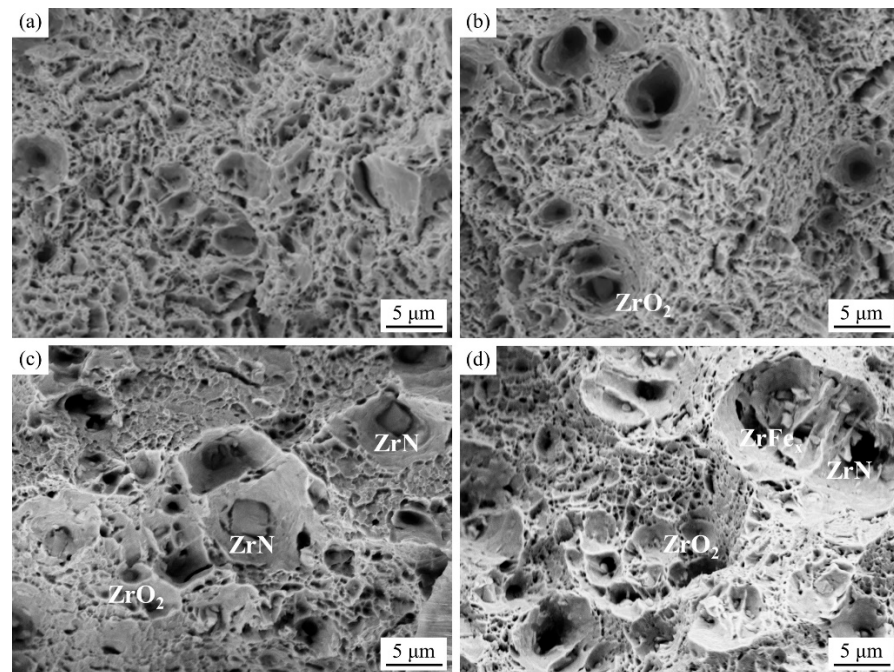

Figure 5. Microscopic fracture morphology of the steels at room temperature. (**a**) 0ZrA, (**b**) 0.004ZrA, (**c**) 0.037ZrA, and (**d**) 0.098ZrA.

3.4. Influences of TMP on Microstructure and Mechanical Property

In order to explore the effect of TMP on the microstructure of 0.004Zr steel, the alloys were treated by Process B, C, D, and E, named as 0.004ZrB, 0.004ZrC, 0.004ZrD, and 0.004ZrE, respectively, and the whole series was defined as the BCDE series. OM and SEM morphologies of TMPed alloys are presented in Figure 6. Typical martensitic structure could be found in all alloys, which indicated that tempered martensite can also be obtained by the TMP process. The prior austenite grains of BCDE series steels measured by the linear intercept method were 22.4, 22.5, 22.3, and 22.4 μm, respectively. Tempering temperature has little effect on grain size. In addition, a large amount of carbides are distributed in crystals and grain boundaries. With the increase in tempering temperature, the precipitates increased gradually. Additionally, the size of precipitates on grain boundaries increases gradually, and the characteristics of martensitic structure become more apparent.
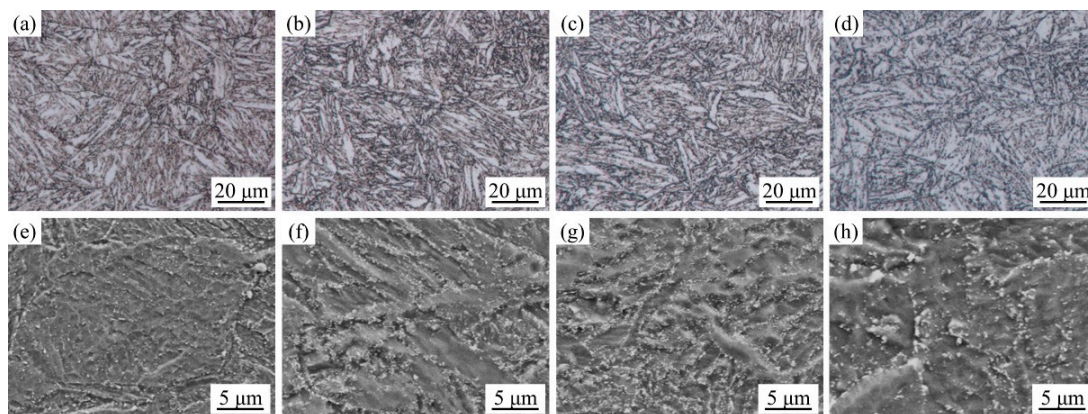

Figure 6. Microstructure morphology of 0.004Zr alloy treated by Process B, C, D, and E. (**a–d**) OM, (**e–h**) SEM, (**a,e**) 0.004ZrB, (**b,f**) 0.004ZrC, (**c,g**) 0.004ZrD, (**d,h**) 0.004ZrE.

Figure 7 shows the OM and SEM morphologies of 0.004Zr alloys treated by Process F, G, H and I, which were named as the FGHI series. The microstructures are tempered martensite. The prior austenite grains of FGHI series steels measured by the linear intercept method were 20.8, 20.9, 22.8, and 22.8 μm, respectively. Based on the SEM morphologies, more precipitates were found in the FGHI series of alloys than the BCDE series. Apart from this, there were no other significant differences between the two series of alloys.
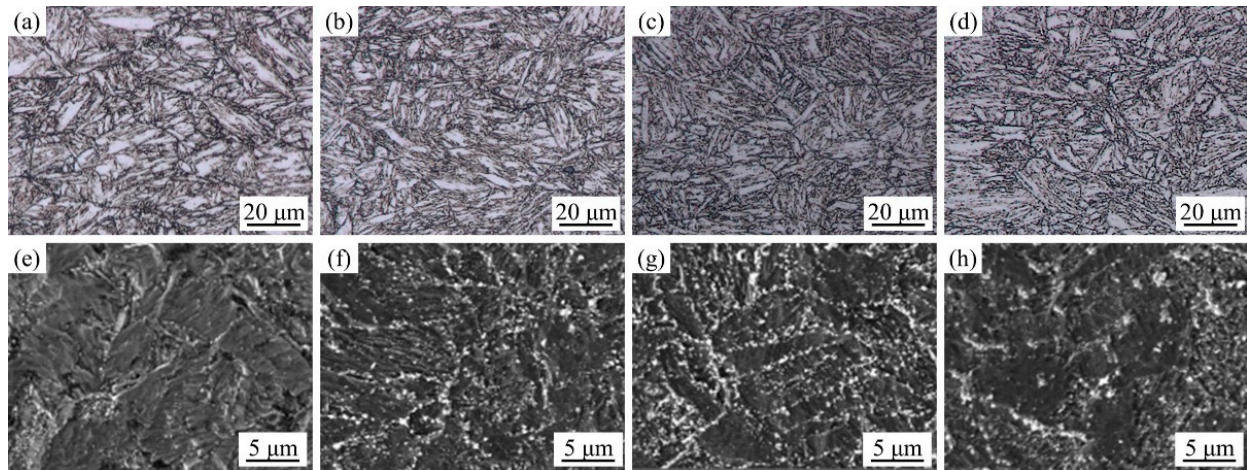

Figure 7. Microstructure morphology of 0.004Zr alloy treated by Process F, G, H and I. (**a–d**) OM, (**e–h**) SEM, (**a,e**) 0.004ZrF, (**b,f**) 0.004ZrG, (**c,g**) 0.004ZrH, (**d,h**) 0.004ZrI.

With the increase in tempering temperature, the yield strength and tensile strength decrease. The specific mechanical properties of 0.004Zr alloy are listed in Table 4. As shown in Table 4, when the tempering temperature was less than 760 °C, the yield strength and tensile strength of FGHI series steel were higher than the BCDE series steel. The lower the tempering temperature, the more apparent this trend. The work hardening effect of the FGHI series alloys was greater than the BCDE series alloys at lower tempering temperatures, which was one of the reasons for these higher strengths. On the other hand, the distortion energy in FGHI series steel was larger than the BCDE series due to the low-temperature rolling, and the atomic activation energy required for solute atom diffusion in steel was smaller during tempering. Therefore, more MX and $M_{23}C_6$ precipitated in FGHI series steel. Moreover, the precipitation strengthening effect of FGHI series steel was better than the BCDE series steel. When the tempering temperature was 795 °C, the steel recovered and recrystallized, and the work hardening effect introduced by rolling was greatly weakened. As a result, the yield strength and tensile strength of FGHI series steel were lower than the BCDE series steel.

Table 4. Mechanical properties of 0.004Zr alloys.

Series	BCDE				FGHI			
Temperature (°C)	690	725	760	795	690	725	760	795
YS (MPa)	863.9	691.6	597.9	537.3	869.6	713.1	611.8	508.2
TS (MPa)	965.7	814.7	726.8	679.3	992.2	832.0	730.0	661.3
Elongation/%	18.9	20.5	24.2	25.9	18.9	20.1	24.7	26.6

Impact energies of BCDE series and FGHI series alloys at room temperature are presented in Figure 8. Impact energies of 0.004ZrB, 0.004ZrC, 0.004ZrD, and 0.004ZrE were 167.4 ± 1.2, 213.8 ± 0.9, 225.9 ± 2.3, and 237.2 ± 1.5 J, respectively, whereas the energies of 0.004ZrF, 0.004ZrG, 0.004ZrH, and 0.004ZrI were 154.6 ± 0.8, 204.5 ± 2.2, 243.3 ± 1.5, and 259.1 ± 2.8 J, respectively. At a tempering temperature of no more than 725 °C, impact energy of 0.004ZrB was larger than 0.004ZrF, and 0.004ZrC was larger than 0.004ZrG. When the tempering temperature was raised to more than 725 °C, the impact energy of

0.004ZrH was larger than 0.004ZrD, and 0.004ZrI was larger than 0.004ZrE. In the process of increasing the tempering temperature, the impact energy of BCDE series steel experienced a process that ranged from being greater than the FGHI series steel to gradually approaching and then being less than the FGHI series steel. With the rise of tempering temperature, the work hardening effect weakened or even eliminated and the steel recovered and statistically recrystallized; thus, the toughness and plasticity of the steel were enhanced. However, since there were more dislocations and vacancies in the FGHI series steel, it was more conducive to the precipitation of carbides and improved the precipitation strengthening effect, which would be responsible for the fine impact performance of 0.004ZrH and 0.004ZrI alloys.
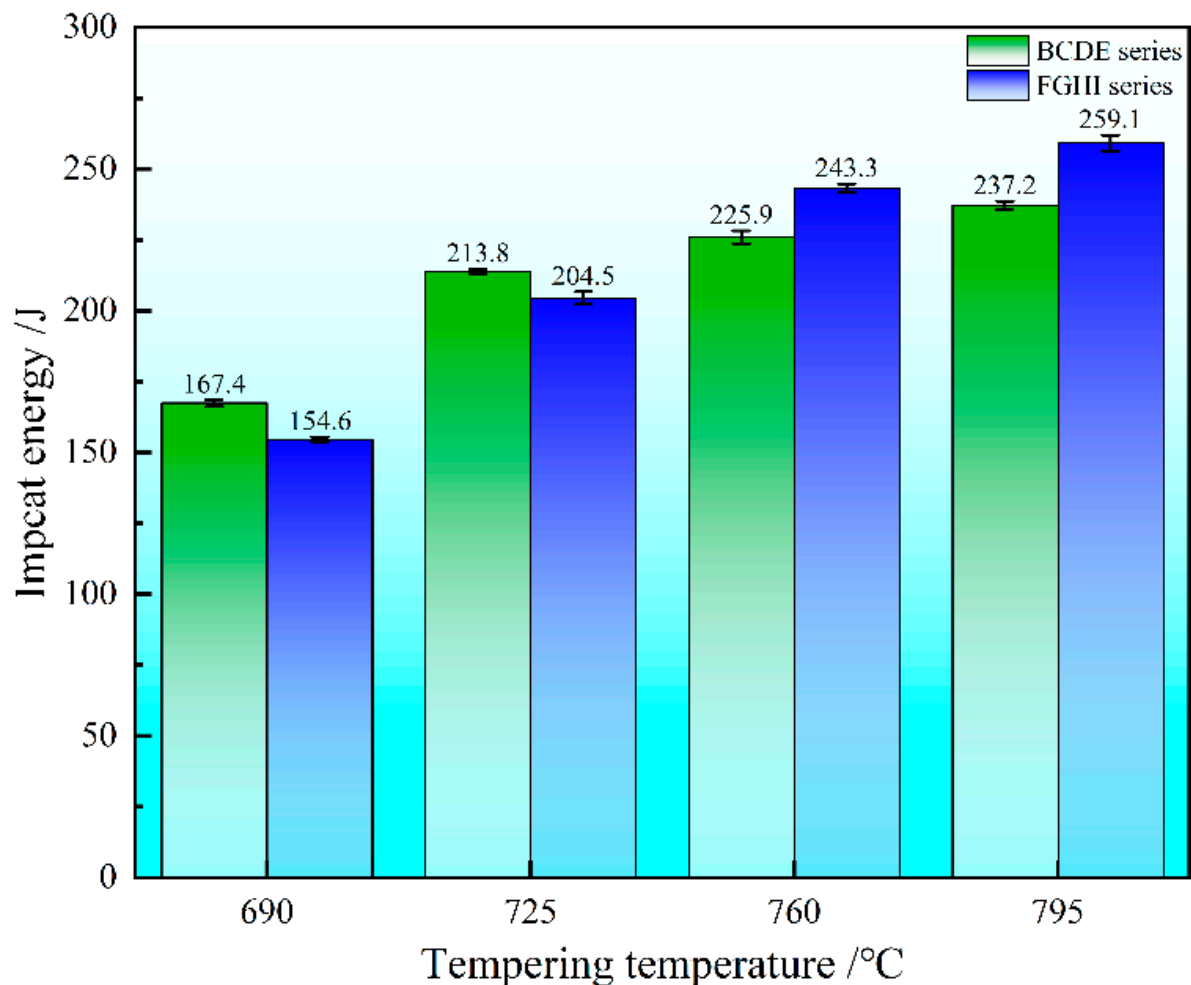

Figure 8. Effect of tempering temperature on the impact energy of alloys.

Figure 9 shows the impact fracture morphology of steel at room temperature. For comparison, the micro morphology of impact fracture was collected in the fiber area. When the tempering temperature was 690 °C, the impact fracture microstructure of 0.004ZrB and 0.004ZrF steels at room temperature showed clear cleavage steps and river patterns, and the fracture mode was quasi-cleavage fracture, as shown in Figure 9a,e. The reason is that there was a large internal stress in the rolled steel, and the low tempering temperature could not eliminate the above internal stress. However, other steels showed ductile fracture characteristics. As a result, 0.004ZrB and 0.004ZrF steels had high strength as well as poor toughness and plasticity. With the increase in TMP temperature, the microstructure of impact fracture of alloys showed the characteristics of ductile fracture. At the same time, the size of dimple in impact fracture increased and deepened.
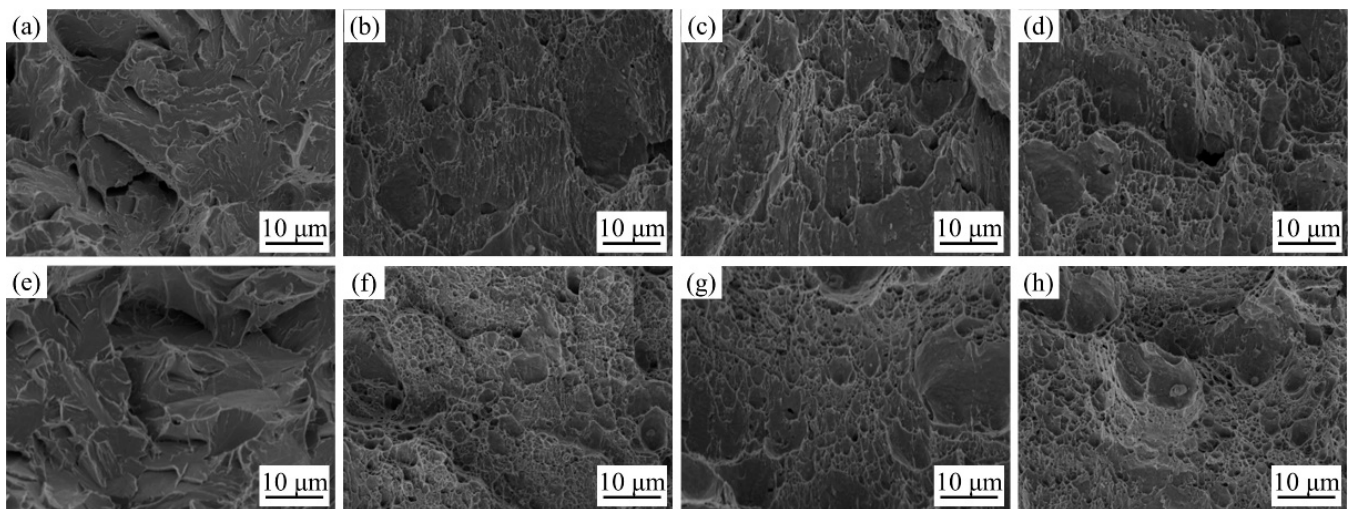
Figure 9. Microscopic morphology of impact fracture under different tempering temperatures. (**a**) 0.004ZrB, (**b**) 0.004ZrC, (**c**) 0.004ZrD, (**d**) 0.004ZrE, (**e**) 0.004ZrF, (**f**) 0.004ZrG, (**g**) 0.004ZrH, and (**h**) 0.004ZrI.

3.5. Effect of Aging on Microstructure and Mechanical Property

It has been found by the analysis that the grain distribution, size, and the precipitated phases of 0.004ZrD and 0.004ZrH have been relatively significantly changed after changing the rolling temperature. In order to further investigate the high-temperature microstructure and strength stability of alloys, the high-temperature thermal aging at 600 °C was carried out with 0.004ZrD and 0.004ZrH steels. The OM of 0.004ZrD steel after aging for 500, 1000, and 1500 h is shown in Figure 10a–c. Prior austenite grain boundary and martensite structure can be observed. The prior austenite grain of 0.004ZrD steel aged for 500, 1000, and 1500 h was 22.8, 23.1, and 23.4 μm, respectively. Although the prior austenite grain boundary can still be observed after aging for 1000 h, the martensite structure becomes unclear. With the further increase in aging time, under the action of thermal activation energy, small-sized austenite grains gradually annex to large-sized austenite grains, which leads to the gradual growth of prior austenite grain boundaries. In addition, with the increase in aging time, a large number of precipitated phases appear. The OM of 0.004ZrH steel aged for different times is presented in Figure 10d–f. Typical martensitic was observed. The prior austenite grains of 0.004ZrH steel aged for 500, 1000, and 1500 h were 21.0, 21.3, and 21.4 μm, respectively. The martensite structure became progressively more challenging to discern as it aged.

Figure 11a–c is the backscatter electron image (BSE) of 0.004ZrD steel aged for different times. With the increase in aging time, more high-contrast precipitates appeared in the aged alloys, which are mainly distributed along the prior austenite grain boundary. The longer the aging time, the greater the density and size of precipitates. In contrast to the $M_{23}C_6$ precipitates, the W-rich Laves phase precipitates can be seen as bright precipitates in the dark matrix; thus, the Laves phase could be clearly distinguished in the BSE images. Figure 11d–f shows the images of 0.004ZrH steel aged at 600 °C for 500, 1000, and 1500 h observed by SEM in BSE. With the increase in aging time, the Laves phase in the steel continuously precipitated. The Laves phase in the 0.004ZrH steel aged for 1500 h is larger than the steels aged for 500 and 1000 h.

Figure 12 presents the surface scan and point analysis results of 0.004ZrD steel aged for 1500 h. It can be clearly seen that the percentage of Fe elements at grain boundaries and sub-grain boundaries decreases as the aging time increases, and the Laves phase forming W elements are enriched at the grain boundaries. This indicates that the higher-contrast precipitates are mainly composed of W. There is no clear segregation of Cr, $M_{23}C_6$ forming element in steel. This may be due to the fact that the precipitation of Laves phase inhibits the coarsening of $M_{23}C_6$ carbide. In addition, the segregation phenomenon of Ta element can

be seen in Figure 12, and the distribution of Ta is similar to W. For martensitic heat-resistant steels, the composition of Laves phase produced during aging is (Fe, Cr)$_2$(Mo, W, Nb, Ti, Ta). According to the chemical composition of the experimental steel, the Laves phase in the experimental steel can be determined as (Fe, Cr)$_2$(W, Ta). Therefore, it can be considered that Ta enriched at grain boundaries is also a type of Laves phase. However, compared with Ta, the segregation caused by the precipitation of W during aging is significantly greater than Ta; namely, Fe$_2$W is the main Laves precipitation phase in long-term high temperature environment, such as high-temperature aging or creep.
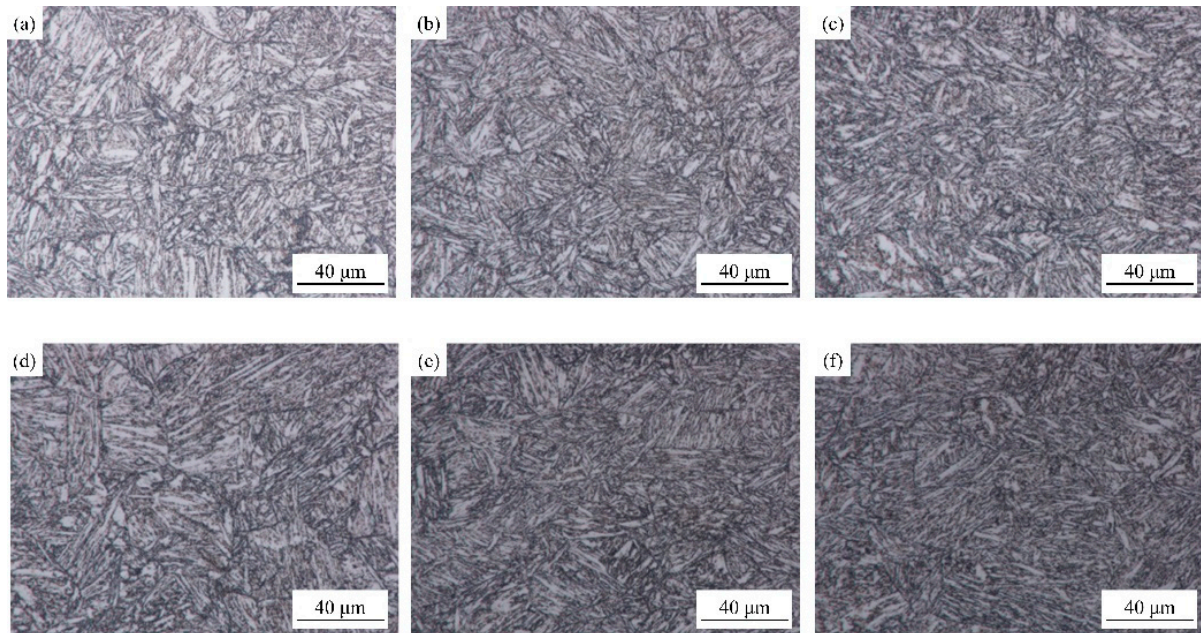
Figure 10. Optical microstructure of 0.004ZrD (**a–c**) and 0.004ZrH (**d–f**) aged for different times (**a,d**) 500 h, (**b,e**) 1000 h, and (**c,f**) 1500 h.
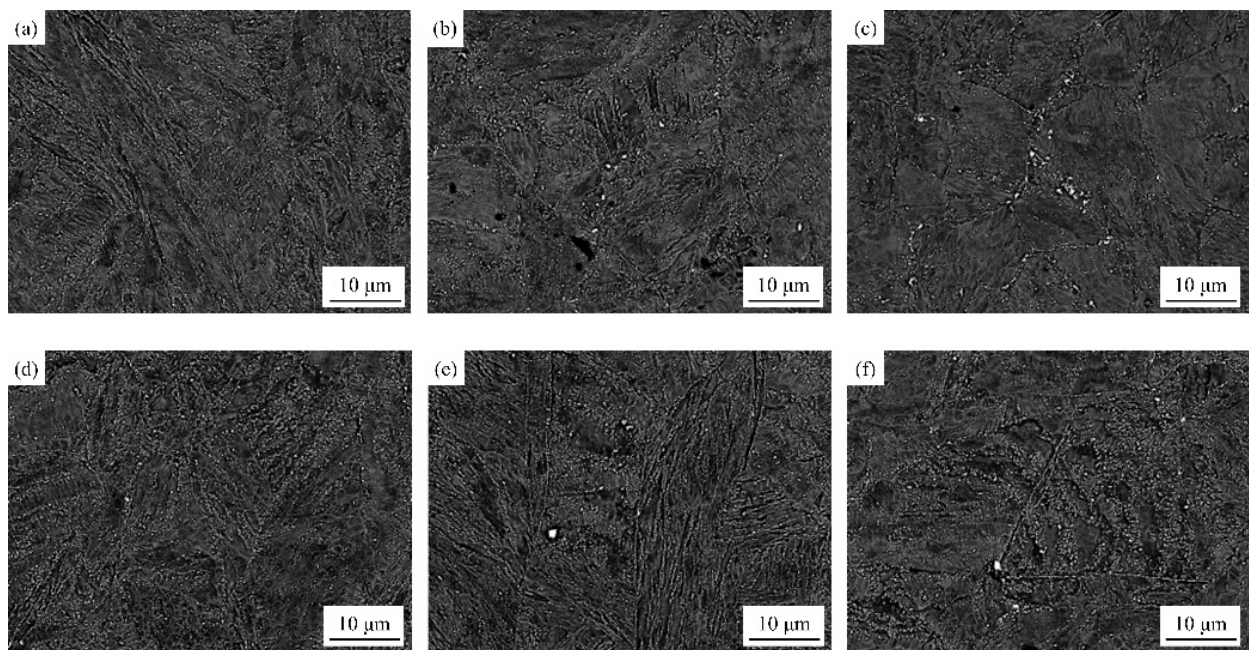

Figure 11. BSE images of 0.004ZrD (**a–c**) and 0.004ZrH (**d–f**) aged for different times (**a,d**) 500 h, (**b,e**) 1000 h, and (**c,f**) 1500 h.
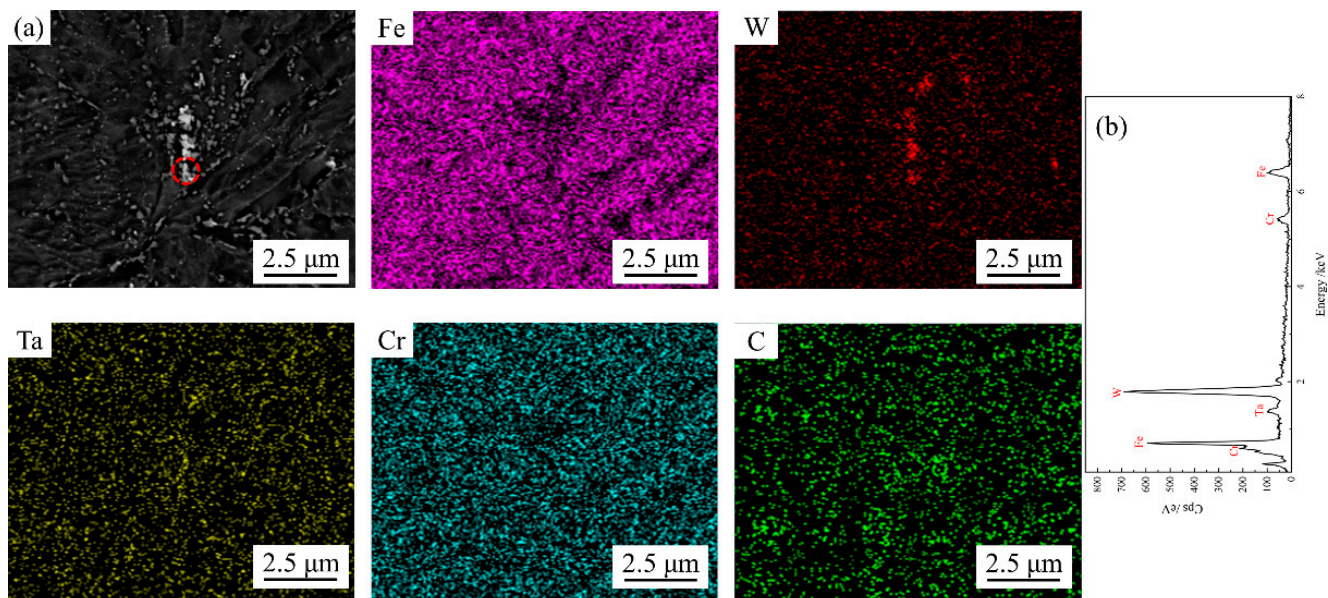
Figure 12. Surface scanning analysis (**a**) of 0.004ZrD aged for 1500 h, (**b**) corresponding result of point analysis of the area indicated in red circle in (**a**).

Table 5 shows the tensile properties of 0.004ZrD steel aged at 600 °C for 500, 1000, and 1500 h. The yield strengths of 0.004ZrD aged for 0, 500, 1000, and 1500 h were 597.9 ± 1.8, 566.1 ± 1.5, 564.6 ± 2.3, and 571.7 ± 1.6 MPa, and the tensile strengths were 726.8 ± 2.7, 708.3 ± 2.5, 699.8 ± 3.0, and 710.5 ± 2.2 MPa, respectively. The 0.004ZrD steel showed good stability of mechanical properties during the aging process. Compared with the unaged steel, the yield strength and tensile strength of the steel aged for 500 h decreased by 18.3 and 31.8 MPa, respectively. This is mainly due to the fact that the work hardening phenomenon caused by hot rolling has not been completely eliminated in the early aging period. When the aging time was less than 500 h, the mechanical properties of the steel decreased slightly. However, when the aging time exceeded 1000 h, the mechanical properties of the steel improved slightly.

Table 5. Mechanical properties of aged 0.004ZrD steel.

Aging Time/h	Yield Strength/MPa	Tensile Strength/MPa	Elongation/%
0	597.9	726.8	24.2
500	566.1	708.3	24.8
1000	564.6	699.8	25.3
1500	571.7	710.5	24.5

With the increase in aging time, the elongation of the alloy increased first and then decreased in the range from 24.2% to 25.3%. Meanwhile, the work hardening effect was further weakened which would be responsible for the increase in elongation and decrease in yield strength of 0.004ZrD aged for 500 h. In addition, with the increase in aging time, the amount of Laves phase precipitation increases, which leads to the decrease in elongation and the increase in yield strength of 0.004ZrD steel aged for 1500 h.

Tensile properties of 0.004ZrH steel aged at 600 °C for 500, 1000, and 1500 h are shown in Table 6. The yield strengths of 0.004ZrH aged for 0, 500, 1000, and 1500 h were 611.8 ± 2.7, 570.2 ± 1.8, 580.2 ± 2.1, and 572.5 ± 1.7 MPa, and the tensile strengths were 730.0 ± 3.3, 709.7 ± 2.3, 708.5 ± 2.7, and 713.4 ± 3.0 MPa, respectively. Moreover, the 0.004ZrH steel showed good mechanical stability during the aging process. When the aging time was 1000 and 1500 h, the mechanical properties of the 0.004ZrF steel were higher than the 0.004ZrD steel.

Table 6. Mechanical properties of aged 0.004ZrH steel.

Aging Time/h	Yield Strength/MPa	Tensile Strength/MPa	Elongation/%
0	611.8	730.0	24.7
500	570.2	709.7	25.4
1000	580.2	708.5	25.9
1500	572.5	713.4	25.5

Similar to the 0.004ZrD steel, the elongation of the 0.004ZrH steel increased first and then decreased with aging time in the range from 24.7% to 25.9%. The higher elongation and yield strength of the aged 0.004ZrF was mainly due to the finer grain size.

Mechanical properties of 0.004ZrD, 0.004ZrH, and other RAFM steels aged at 650 °C for 1500 h are shown in Figure 13. The TMPed alloys had higher yield and tensile strengths than the other quenched and tempered RAFM steels (CLAM [24], F82H [1], and Zr-RAFM [25]). The yield strength was ~98 MPa higher than the CLAM steel, ~123 MPa higher than the F82H steel, and ~48 MPa higher than the Zr-RAFM steel. The tensile strength was ~88 MPa higher than the CLAM steel, ~138 MPa higher than the F82H steel, and ~128 MPa higher than the Zr-RAFM steel. The present study showed that TMP is simple and readily applicable to the industry, which can effectively improve the strength of RAFM steels.
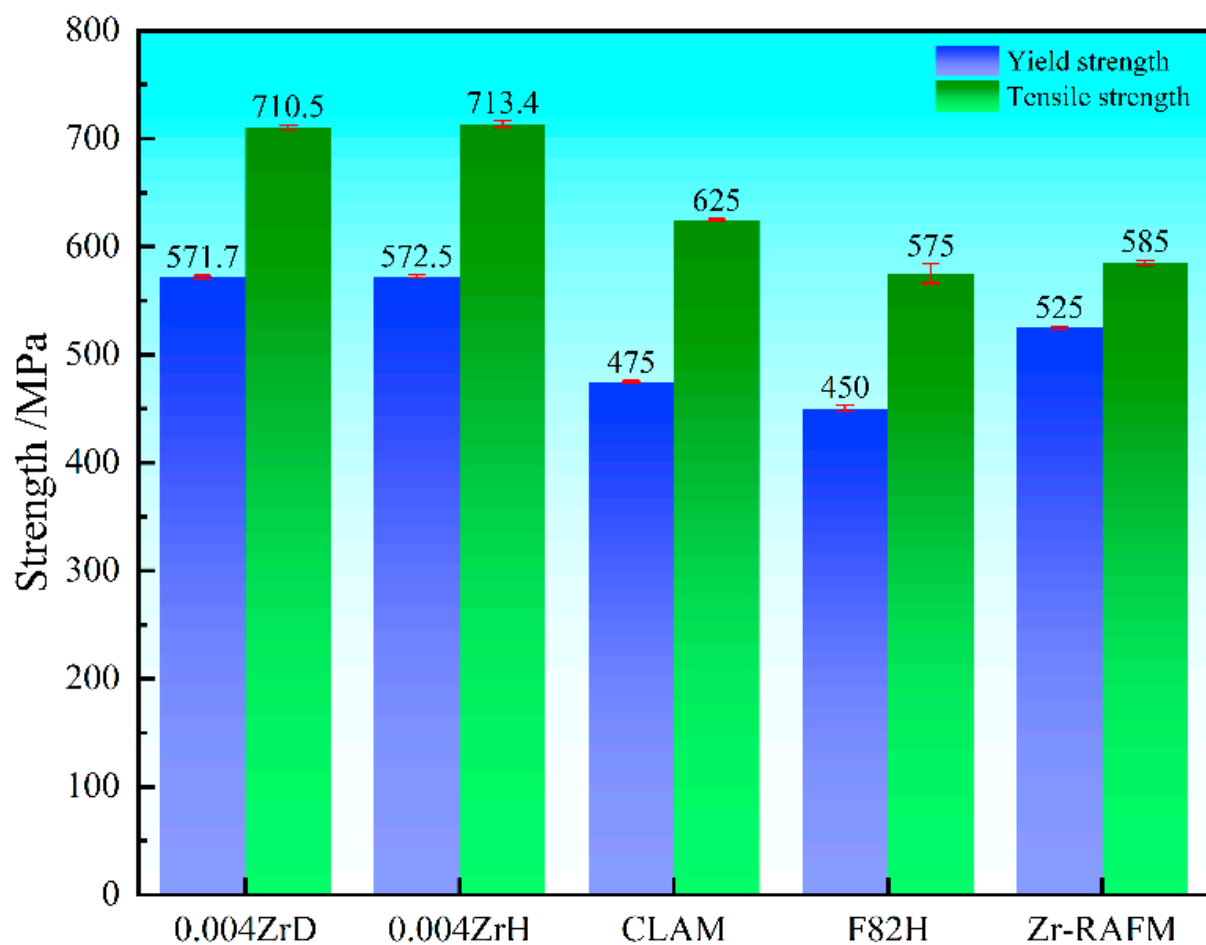
Figure 13. Mechanical properties of aged 0.004ZrD, 0.004ZrH, and other aged RAFM steels.

4. Conclusions

(1) The inclusions in CLAM steel with Zr could be divided into fine simple particles and large complex particles. Typical simple particles include TaO_x, MnS, and ZrN

and complex particles were TaO_x-ZrO_2, ZrO_2-MnS, TaO_x-ZrN, and $FeZr_x$-ZrO_2. The higher the Zr content, the more complex the composition of inclusions in the alloy.

(2) CLAM steel with 0.004% Zr (0.004Zr) had the highest yield strength, tensile strength, elongation, and impact energy at room temperature, which were 548.3 MPa, 679.4 MPa, 25.7%, and 253.9 J, respectively. The main precipitates in 0.004Zr steel were MX and $M_{23}C_6$. With the addition of Zr content in the alloys, the strength and toughness decreased due to the larger inclusions.

(3) With the increase in tempering temperature, the yield strength and tensile strength of TMPed steels gradually decreased, while the elongation and impact energy gradually increased. The optimum yield strength and impact energy belonged to the 0.004ZrD and 0.004ZrH alloys. The yield strengths were 597.9 and 611.8 MPa, while the impact energies were 225.9 and 243.3 J, respectively.

(4) During aging at 650 °C for 1500 h, the Laves phase precipitated and coarsened continuously, and the yield strength of 0.004ZrD and 0.004ZrH alloys decreased and then tended to stabilize. The yield strength of 0.004ZrD changed from 564.6 to 597.9 MPa, and the yield strength of 0.004ZrH changed from 570.2 to 611.8 MPa. TMP is a simple and practical industrial technique that could successfully enhance the mechanical properties of alloys.

Data Availability Statement: The raw/processed data required to reproduce these findings cannot be shared at this time as the data are related to an ongoing study.

Conflicts of Interest: The authors declare no conflict of interest.

References

1. Nagasaka, T.; Ando, M.; Tanigawa, H.; Sakasegawa, H.; Tanaka, T.; Muroga, T.; Sagara, A. Tensile properties of F82H steel after aging at 400–650 °C for 1000–30,000 h. *Fusion Eng. Des.* **2017**, *124*, 1011–1014. [CrossRef]
2. Qiu, G.X.; Zhan, D.P.; Cao, L.; Jiang, Z.H. Review on development of reduced activated ferritic/martensitic steel for fusion reactor. *J. Iron Steel Res. Int.* **2022**, *29*, 1343–1356. [CrossRef]
3. Lindau, R.; Möslang, A.; Rieth, M.; Klimiankou, M.; Materna-Morris, E.; Alamo, A.; Tavassoli, A.-A.F.; Cayron, C.; Lancha, A.-M.; Fernandez, P.; et al. Present development status of EUROFER and ODS-EUROFER for application in blanket concepts. *Fusion Eng. Des.* **2005**, *7579*, 989–996. [CrossRef]
4. Abe, F. Precipitate Design for creep strengthening of 9% Cr tempered martensitic steel for ultra-supercritical power plants. *Sci. Technol. Adv. Mater.* **2008**, *9*, 013002. [CrossRef] [PubMed]
5. Liu, S.J.; Huang, Q.Y.; Li, C.J.; Bo, H. Influence of non-metal inclusions on mechanical properties of CLAM steel. *Fusion Eng. Des.* **2009**, *84*, 1214–1218. [CrossRef]
6. Liao, H.; Wang, X.; Yang, G.; Feng, Y.; Wang, P.; Feng, K. Recent progress of R&D activities on reduced activation ferritic/martensitic steel (CLF-1). *Fusion Eng. Des.* **2019**, *147*, 111235.
7. Mazzone, G.; Aktaa, J.; Bachmann, C.; De Meis, D.; Frosi, P.; Gaganidze, E.; Di Gironimo, G.; Mariano, G.; Marzullo, D.; Porfiri, M.T.; et al. Choice of a low operating temperature for the DEMO EUROFER97 divertor cassette. *Fusion Eng. Des.* **2017**, *124*, 655–658. [CrossRef]
8. Sakasegawa, H.; Tanigawa, H. Mechanical properties of F82H plates with different thicknesses. *Fusion Eng. Des.* **2016**, *109–111*, 1724–1727. [CrossRef]
9. Klueh, R.L.; Sokolov, M.A. Mechanical properties of irradiated 9Cr-2WVTa steel with and without nickel. *J. Nucl. Mater.* **2007**, *367*, 102–106. [CrossRef]

10. Rogozhkin, S.V.; Ageev, V.S.; Aleev, A.A.; Zaluzhnyi, A.G.; Leont'eva-Smirnova, M.V.; Nikitin, A.A. Tomographic atom-probe analysis of temperature-resistant 12%-chromium ferritic-martensitic steel EK-181. *Phys. Met. Metallogr.* **2009**, *108*, 579–585. [CrossRef]

11. Chun, Y.B.; Lee, D.W.; Cho, S.; Rhee, C.K. Improvement of creep and impact resistance of reduced activation ferritic-martensitic steel by the addition of Zr. *Mater. Sci. Eng. A* **2015**, *645*, 286–291. [CrossRef]

12. Guo, A.M.; Li, S.R.; Guo, J.; Li, P.H.; Ding, Q.F.; Wu, K.M.; He, X.L. Effect of zirconium addition on the impact toughness of the heat affected zone in a high strength low alloy pipeline steel. *Mater. Charact.* **2008**, *59*, 134–139. [CrossRef]

13. Park, J.W.; Lee, K.K.; Jung, W.S. Elevated temperature deformation behavior of low carbon ZR-B steel. *Scr. Mater.* **2001**, *44*, 587–592. [CrossRef]

14. Chun, Y.B.; Kang, S.H.; Lee, D.W.; Cho, S.; Jeong, Y.H.; Żywczak, A.; Rhee, C.K. Development of Zr-containing advanced reduced-activation alloy (ARAA) as structural material for fusion reactors. *Fusion Eng. Des.* **2016**, *109–111*, 629–633. [CrossRef]

15. Tanigawa, H.; Gaganidze, E.; Hirose, T.; Ando, M.; Zinkle, S.; Lindau, R.; Diegele, E. Development of benchmark reduced activation ferritic/martensitic steels for fusion energy applications. *Nucl. Fusion* **2017**, *57*, 092004. [CrossRef]

16. Zinkle, S.; Boutard, J.; Hoelzer, D.; Kimura, A.; Lindau, R.; Odette, G.; Rieth, M.; Tan, L.; Tanigawa, H. Development of next generation tempered and ODS reduced activation ferritic/martensitic steels for fusion energy applications. *Nucl. Fusion* **2017**, *57*, 092005. [CrossRef]

17. Chun, Y.B.; Rhee, C.K.; Lee, D.W.; Park, Y.H. Enhanced high-temperature mechanical properties of ARAA by thermomechanical processing. *Fusion Eng. Des.* **2018**, *136*, 883–890. [CrossRef]

18. Karasev, A.; Suito, H. Analysis of Size Distributions of Primary Oxide Inclusions in Fe-10 Mass Pct Ni-M (M=Si, Ti, Al, Zr, and Ce) Alloy. *Metall. Mater. Trans. B* **1999**, *30*, 259–270. [CrossRef]

19. Zhou, J.H.; Shen, Y.F.; Jia, N. Strengthening mechanisms of reduced activation ferritic/martensitic steels: A review. *Int. J. Miner. Metall. Mater.* **2021**, *28*, 335–348. [CrossRef]

20. Qiu, G.X.; Zhan, D.P.; Li, C.S.; Qi, M.; Jiang, Z.; Zhang, H. Effect of Y/Zr Ratio on Inclusions and Mechanical Properties of 9Cr-RAFM Steel Fabricated by Vacuum Melting. *J. Mater. Eng. Perform.* **2019**, *28*, 1067–1076. [CrossRef]

21. Gurland, J.; Plateau, J. Mechanism of ductile rupture of metals containing inclusions. *Copper Alloys* **1963**, *56*, 442–454.

22. Shi, Z.; Han, F. The microstructure and mechanical properties of micro-scale Y_2O_3 strengthened 9Cr steel fabricated by vacuum casting. *Mater. Des.* **2015**, *66*, 304–308. [CrossRef]

23. Yan, W.; Hu, P.; Wang, W.; Zhao, L.; Shan, Y.; Yang, K. Effect of yttrium on mechanical properties of 9Cr-2WVTa low active martensite steel. *Chin. J. Nucl. Sci. Eng.* **2009**, *29*, 50–55.

24. Hu, X.; Huang, L.; Yan, W.; Wang, W.; Sha, W.; Shan, Y.; Yang, K. Evolution of microstructure and changes of mechanical properties of CLAM steel after long-term aging. *Mater. Sci. Eng. A* **2013**, *586*, 253–258. [CrossRef]

25. Qiu, G.X.; Zhan, D.P.; Cao, L.; Zhang, H.S. Effect of zirconium on inclusions and mechanical properties of China low activation martensitic steel. *J. Iron Steel Res. Int.* **2021**, *28*, 1168–1179. [CrossRef]